Ordinary state-based peridynamic shell model with arbitrary horizon domains for surface effect correction

Ming-Jyun Dai[a], Satoyuki Tanaka[a,*], Pai-Chen Guan[b], Selda Oterkus[c], Erkan Oterkus[c]

[a] *Graduate School of Advanced Science and Engineering, Hiroshima University, Japan*
[b] *Department of Systems Engineering and Naval Architecture, National Taiwan Ocean University, Taiwan*
[c] *Department of Naval Architecture, Ocean and Marine Engineering, University of Strathclyde, United Kingdom*

Abstract

An ordinary state-based peridynamic (PD) shell model with arbitrary horizon domains is presented. In the computation of PD parameters, the model removes the complete horizon assumption to treat the PD surface effect. In this study, the membrane, bending, and transverse shear deformations of the PD shell model are taken into account. To examine fracture mechanics behavior, crack opening displacements and strain energy densities, which correspond to physical values of the PD failure criteria, are investigated under single- and mixed-mode fracture conditions. Several numerical examples are considered to evaluate fracture behaviors for shell structures subjected to in-plane or out-of-plane loading. The PD surface effect near domain boundaries or crack surfaces is validly treated by using the presented method. In addition, a crack propagation analysis is performed to estimate the effectiveness of the presented method.

Keywords: Peridynamics; Thin-walled structures; Arbitrary horizon domain; Surface effect; Crack propagation

*Corresponding author. E-mail addresses: mingjyundai@gmail.com (M.J. Dai), satoyuki@hiroshima-u.ac.jp (S. Tanaka), paichen@mail.ntou.edu.tw (P.C. Guan), selda.oterkus@strath.ac.uk (S. Oterkus), erkan.oterkus@strath.ac.uk (E. Oterkus)

1. Introduction

A nonlocal theory, peridynamics (PD) [1,2], provides an alternative approach to deal with fracture mechanics problems. In contrast to classical continuum mechanics (CCM), the PD theory does not involve spatial derivatives in its governing equations. Hence, it is well suited to treat complicated fracture problems without additional numerical techniques. Three different types of PD formulations have been proposed in the PD literature, specifically, bond-based PD (BBPD) [1], ordinary state-based PD (OSPD) [2], and non-ordinary state-based PD (NOSPD) [2]. BBPD places constraints on material properties and plastic behavior. Poisson's ratio is restricted to specified values. Moreover, the volumetric strain is merely considered in permanent deformation; hence, it is inconsistent with plastic incompressibility in metals. Therefore, OSPD and NOSPD have been subsequently developed as more general forms to relax limitations placed on material properties and plastic behavior.

Because of their high strength-to-weight ratio, thin-walled structures are commonly used in aerospace and maritime industries. In the PD framework, each material point interacts with the other material points within a specified region. The nonlocal interactions lead to lower efficiency of computational effort, especially for 3D PD models. To simulate thin-walled structures, structural idealization is one of the approaches to reduce computation time. The Kirchhoff–Love plate [3,4], the Mindlin–Reissner plate [5], and the shell [6,7] models have been proposed in the PD literature. Furthermore, several engineering applications of thin-walled structures in PD have been reported concerning buckling [8], vibration [9], stress intensity factor [10,11], composite material [12,13], ship strength [14], and nonlinear [15] problems.

In CCM, crack opening displacement (COD), stress intensity factors, and J-integral are the main failure criteria to determine the status of crack propagation at the crack tip. In the PD framework, cracking is dictated by the status of interaction bonds between material points. Several failure criteria that concern critical values of interaction bonds can be found in the previous PD studies. Silling and Askari [16] introduced a failure criterion based on bond elongation, which is called the critical bond stretch. This criterion only involving the volumetric deformation is insensitive to the deviatoric deformation. It is mainly applied to mode-I fracture problems in brittle materials. Subsequently, two energy-based failure criteria, called the critical energy density, were proposed in Refs. [17] and [18] to overcome underestimates in the

critical bond stretch. Dipasquale and collaborators [19] examined the effectiveness of the failure criteria mentioned above in mixed-mode fracture problems. Moreover, COD [20], energy release rate [21], equivalent strain [22], and the Johnson-Cook damage model [23] were introduced into the PD framework to predict fracture behaviors.

The PD surface effect arises from the assumption that PD parameters are computed based on a complete horizon. If the material point is located near domain boundaries or crack surfaces, the complete horizon assumption is not satisfied. Therefore, the accuracy of computational results in BBPD and OSPD are strongly affected. Le and Bobaru [24] investigated 2D linear elastic and fracture problems with different surface effect corrections. In most surface effect corrections, the PD force density is corrected by multiplying a correction factor to reduce the PD surface effect. The correction factor is obtained by comparing some physical quantities between the complete and present horizons. Such correction methods only reduce the surface effect rather than eliminate it. The fictitious node method [25] can well eliminate the surface effect in simple geometries. However, it meets severe challenges in complex geometries, in particular, for configured models with cracks. An alternative approach to minimize the PD surface effect has been presented by using arbitrary horizon domains. Queiruga and Moridis [26] performed a convergence analysis with three state-based PD models. In one of the presented models, its PD parameters were evaluated employing arbitrary horizon domains. Chen [27] presented a similar approach to deal with 2D static and dynamic problems. Madenci and collaborators proposed a PD truss element in the finite element framework [28] and a weak form of PD governing equations [29]. Both proposed methods are free of the PD surface effect by using variable horizons. Only 2D problems were taken into account in the reference studies mentioned above [26-29]. For the surface effect treatment with arbitrary horizon domains, out-of-plane deformations for thin-walled structures still have been not discussed.

The capabilities of the adopted OSPD shell model were examined in several numerical investigations [6,10,11,14]. For this reason, the PD shell model is employed in the present study to assess fracture mechanics behaviors subjected to in-plane or out-of-plane loading. Moreover, the arbitrary horizon domain method [26,27] is introduced into the PD framework to treat the PD surface effect. For the surface effect treatment, the membrane, bending, and transverse shear terms are considered in the computation of PD parameters. To examine the effectiveness of the proposed method, CODs and

strain energy densities (SEDs) that correspond respectively to the critical bond stretch [16] and critical energy density [17,18] criteria are investigated. Finally, a crack propagation analysis of a diagonally loaded square plate (DLSP) specimen [30] is simulated.

The remainder of the paper is organized as follows. The PD shell model and its numerical implementations are introduced in Section 2. The arbitrary horizon domain method for shell structures is presented in Section 3. Several numerical problems are demonstrated in Section 4. The conclusions are given in Section 5.

2. Ordinary state-based peridynamic theory

2.1. Peridynamic model for shell structures

The OSPD model for shell structures [6] is adopted in the present study. A schematic illustration of the PD shell model is presented in Fig. 1. $\boldsymbol{x}_{(k)}$ and $\boldsymbol{y}_{(k)}$ denote the initial and deformed positions of point k, respectively. φ represents the angle of the interaction bond between points k and j with respect to the x_1-axis. h indicates the shell thickness. $\boldsymbol{u}_{(k)}=[u\ v\ w\ \theta_x\ \theta_y]^T$ denotes the displacement vector for five degrees of freedom. $\boldsymbol{t}_{(k)(j)}$ and $\boldsymbol{t}_{(j)(k)}$ represent the PD force density vectors between points k and j.

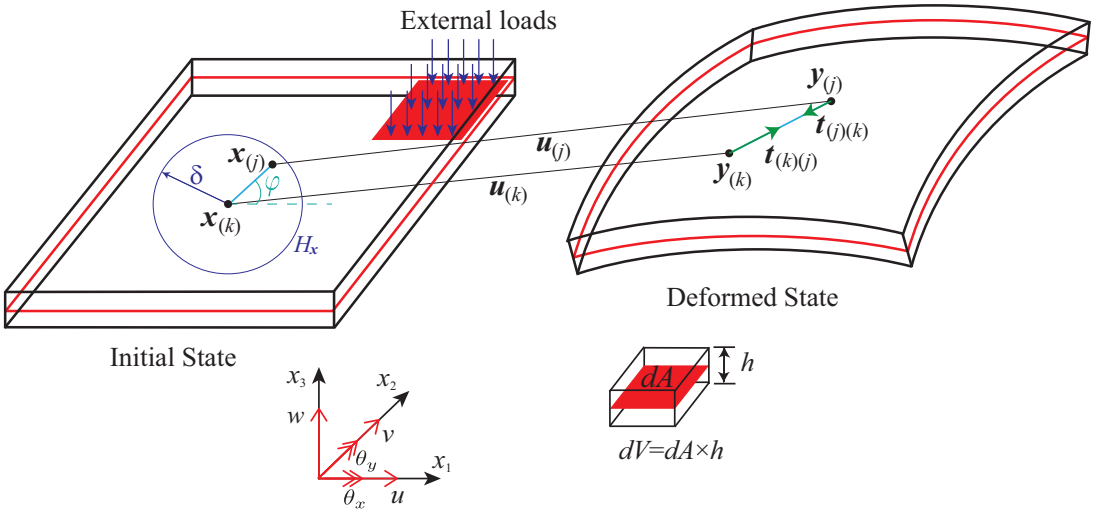

Figure 1: Initial and deformed states of a flat shell in PD.

The PD SEDs are obtained by summing micro-potentials of all material points within the specified area, H_x. The micro-potential depends on the bond stretch and constitutive properties of each interaction bond. For the OSPD shell model, the SEDs composed of the membrane, bending, and transverse shear terms are defined as

$$\bar{W}^{PD}_{ip(k)} = a_{ip}\vartheta^2_{ip(k)} + b_{ip}\sum_{j=1}^{N}\underline{w}s^2_{ip(k)(j)}\xi^2 V_{(j)}, \tag{1}$$

$$\bar{W}^{PD}_{b(k)} = a_{b}\vartheta^2_{b(k)} + b_{b}\sum_{j=1}^{N}\underline{w}s^2_{b(k)(j)}\xi^2 V_{(j)}, \tag{2}$$

$$\bar{W}^{PD}_{s(k)} = \frac{1}{4}C_s\sum_{j=1}^{N}\underline{w}(\frac{w_{(j)} - w_{(k)}}{\xi} - \frac{\bar{\theta}_{(j)} + \bar{\theta}_{(k)}}{2})^2\xi^2 V_{(j)}, \tag{3}$$

where s, ϑ, and ξ denote the bond stretch, dilatation, and distance between points k and j, respectively. $\bar{\theta}_{(k)}$ and $\bar{\theta}_{(j)}$ represent the rotations with respect to the interaction bond. N indicates the total number of material points within H_x. The influence function $\underline{w}$=δ/ξ is defined. a, b, d, and C denote the PD parameters. Subscripts ip, b, and s to the PD parameters signify that the quantities relate to the membrane, bending, and transverse shear terms, respectively.

Bond stretch s is the relative deformation of the interaction bond, and dilatation ϑ is the relative volume variation of the material point. Bond stretches s_{ip} and s_b for the membrane and bending deformations are defined as

$$s_{ip(k)(j)} = \frac{(u_{(j)} - u_{(k)})\cos\varphi + (v_{(j)} - v_{(k)})\sin\varphi}{\xi}, \tag{4}$$

$$s_{b(k)(j)} = \frac{-(\theta_{y(j)} - \theta_{y(k)})\cos\varphi + (\theta_{x(j)} - \theta_{x(k)})\sin\varphi}{\xi}. \tag{5}$$

Dilatations ϑ_{ip} and ϑ_b for the membrane and bending deformations are defined as

$$\vartheta_{ip(k)} = d_{ip} \sum_{j=1}^{N} \underline{w} s_{ip(k)(j)} \xi V_{(j)}, \tag{6}$$

$$\vartheta_{b(k)} = d_b \sum_{j=1}^{N} \underline{w} s_{b(k)(j)} \xi V_{(j)}. \tag{7}$$

Rotations $\bar{\theta}_{(k)}$ and $\bar{\theta}_{(j)}$ with respect to the interaction bond between points k and j are defined as

$$\bar{\theta}_{(k)} = -\theta_{y(k)} \cos\varphi + \theta_{x(k)} \sin\varphi, \tag{8}$$

$$\bar{\theta}_{(j)} = -\theta_{y(j)} \cos\varphi + \theta_{x(j)} \sin\varphi. \tag{9}$$

The PD parameters are obtained by comparing dilatations and SEDs between CCM and PD under simple loading conditions. The PD parameters for the membrane, bending, and transverse shear terms are expressed as

$$a_{ip} = \frac{Eh(3\nu - 1)}{4(1 - \nu^2)}, \quad d_{ip} = \frac{3E}{\pi\delta^4(1 + \nu)}, \quad b_{ip} = \frac{2}{\pi h \delta^3}, \tag{10}$$

$$a_b = \frac{Eh^3(3\nu - 1)}{48(1 - \nu^2)}, \quad d_b = \frac{Eh^2}{4\pi\delta^4(1 + \nu)}, \quad b_b = \frac{2}{\pi h \delta^3}, \tag{11}$$

$$C_s = \frac{3k_s E}{\pi\delta^4(1 + \nu)}, \tag{12}$$

where E, ν, k_s, and δ denote Young's modulus, Poisson's ratio, shear correction factor, and horizon radius, respectively.

The potential energy arises from SEDs and work done by body forces. By substituting the kinetic and potential energies into the Euler-Lagrange equation, the PD equation of motion, which is an integro-differential equation without spatial derivatives, is yielded as

$$\begin{aligned}\boldsymbol{m}_{(k)}\ddot{\boldsymbol{u}}_{(k)} &= \int_{H_x} (\boldsymbol{t}_{(k)(j)} - \boldsymbol{t}_{(j)(k)}) V_{(j)} + \boldsymbol{b}_{(k)} \\ &= \int_{H_x} \boldsymbol{f}_{(k)(j)} V_{(j)} + \boldsymbol{b}_{(k)},\end{aligned} \tag{13}$$

where $\boldsymbol{m}_{(k)}$, $\ddot{\boldsymbol{u}}_{(k)}$, and $\boldsymbol{b}_{(k)}$ denote the mass matrix, acceleration vector, and body force vector, respectively. $\boldsymbol{f}_{(k)(j)}$=$\boldsymbol{t}_{(k)(j)}$-$\boldsymbol{t}_{(j)(k)}$ represents the PD force density vector, and $V_{(j)}$ indicates the volume of point j. The PD equation of motion is briefly introduced here. Its derivation can be found in detail in Ref. [31]. Note that, in the proposed PD model, an assumption stipulating small deformations is imposed.

Material behavior exhibited in the PD framework is described by integrating nonlocal force interactions between material points. The nonlocal force densities are derived from the derivation of the PD equation of motion. The PD force densities for each degree of freedom in the OSPD shell model are expressed as

$$f^{u}_{(k)(j)} = [2a_{ip}d_{ip}\underline{w}(\vartheta_{ip(k)} + \vartheta_{ip(j)}) + 4b_{ip}\underline{w}s_{ip(k)(j)}\xi]\cos\varphi, \tag{14}$$

$$f^{v}_{(k)(j)} = [2a_{ip}d_{ip}\underline{w}(\vartheta_{ip(k)} + \vartheta_{ip(j)}) + 4b_{ip}\underline{w}s_{ip(k)(j)}\xi]\sin\varphi, \tag{15}$$

$$\begin{aligned}f^{w}_{(k)(j)} =& C_s\underline{w}\{\frac{w_{(j)} - w_{(k)}}{\xi} - \frac{1}{2}[-(\theta_{y(k)} + \theta_{y(j)})\cos\varphi \\ &+ (\theta_{x(k)} + \theta_{x(j)})\sin\varphi]\}\xi,\end{aligned} \tag{16}$$

$$\begin{aligned}f^{\theta_x}_{(k)(j)} =& [2a_bd_b\underline{w}(\vartheta_{b(k)} + \vartheta_{b(j)}) + 4b_b\underline{w}s_{b(k)(j)}\xi]\sin\varphi \\ &+ \frac{1}{2}C_s\underline{w}\{(w_{(j)} - w_{(k)})\sin\varphi \\ &- \frac{\xi}{2}[-(\theta_{y(k)} + \theta_{y(j)})\sin\varphi\cos\varphi + (\theta_{x(k)} + \theta_{x(j)})\sin^2\varphi]\}\xi,\end{aligned} \tag{17}$$

$$
\begin{aligned}
f^{\theta_y}_{(k)(j)} = & -\left[2a_b d_b \underline{w}(\vartheta_{b(k)} + \vartheta_{b(j)}) + 4b_b \underline{w} s_{b(k)(j)} \xi\right] \cos\varphi \\
& - \frac{1}{2} C_s \underline{w} \{(w_{(j)} - w_{(k)}) \cos\varphi \\
& - \frac{\xi}{2}[-(\theta_{y(k)} + \theta_{y(j)}) \cos^2\varphi + (\theta_{x(k)} + \theta_{x(j)}) \sin\varphi \cos\varphi]\}\xi.
\end{aligned} \tag{18}
$$

2.2. Surface effect correction and volume correction

Several numerical techniques are introduced within the PD shell framework to improve the accuracy of computational results, including surface effect correction [24] and volume correction [31]. Meanwhile, the state of interaction bonds is also employed to model crack segments. Therefore, the PD equation of motion is rewritten as

$$
\boldsymbol{m}_{(k)} \ddot{\boldsymbol{u}}_{(k)} = \sum_{j=1}^{N} \mu_{(k)(j)} \lambda \boldsymbol{f}_{(k)(j)} \upsilon V_{(j)} + \boldsymbol{b}_{(k)}, \tag{19}
$$

where $\mu_{(k)(j)}$ denotes the state of each interaction bond. λ and υ represent the correction factors for surface effect correction and volume correction, respectively. For static and quasi-static problems, the adaptive dynamic relaxation technique [31] is adopted in PD computations.

Although the volume method for surface effect correction is based on the premise of the homogeneous expansion, it is a simple and effective approach to reduce the PD surface effect [24]. The volume method is chosen as one of the approaches in the present study. A schematic illustration of the volume method is shown in Fig. 2(a). In the volume method, the PD force density for each interaction bond is revised by multiplying a correction factor. The correction factor λ is defined as the ratio of the complete horizon volume to the present horizon volumes; specifically,

$$
\lambda = \frac{2V_0}{V_{(k)} + V_{(j)}}, \tag{20}
$$

where $V_0{=}\pi\delta^2 h$ denotes the volume of the complete horizon, and $V_{(k)}$ and $V_{(j)}$ denote the volumes of the present horizons at points k and j, respectively.

For nonlocal interactions between material points, the material point in the vicinity of the horizon boundary only possesses a partial volume (see Fig.

2(b)). The blue and green regions signify that the material point possesses complete and partial volumes, respectively. The volume correction [31] is adopted to amend the volumes of material points within H_x. The volume correction factor υ is defined as

$$\upsilon = \begin{cases} 1, & \xi < \delta - r, \\ (\delta + r - \xi)/2r, & \delta - r < \xi < \delta, \\ 0, & \delta < \xi, \end{cases} \tag{21}$$

where r=$\Delta x/2$ is defined.

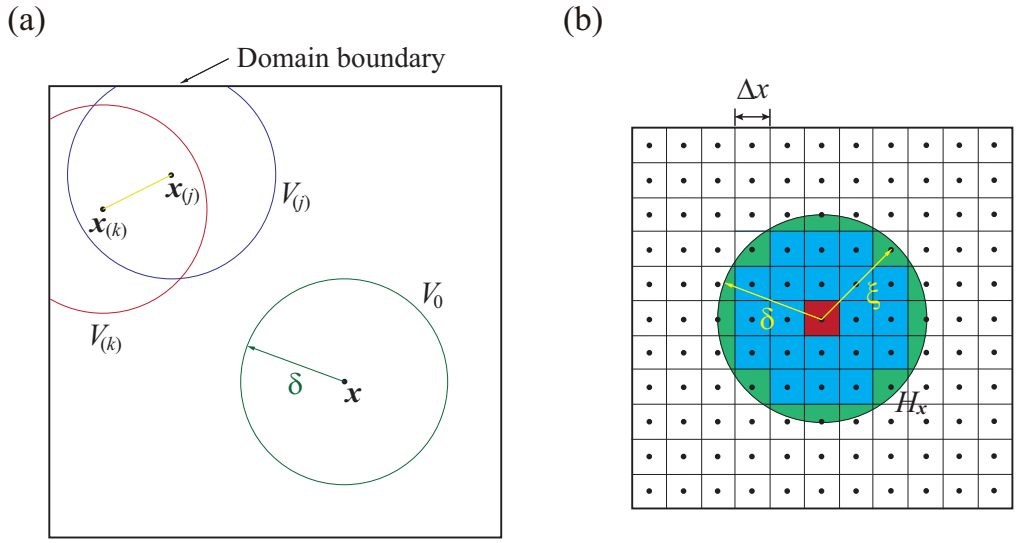

Figure 2: Surface effect correction and volume correction, (a) Volume method for surface effect correction, (b) Volume correction.

2.3. PD failure criteria

Here, the critical bond stretch [16] and critical energy density [17] criteria for interaction bonds are introduced. The critical bond stretch is the most popular failure criterion in the PD literature. The interaction bond between material points breaks once the bond stretch exceeds its critical value. The critical value is yielded from the total work required to eliminate all interactions across a newly created crack surface. The critical bond stretch in OSPD is expressed as

$$s_c = \sqrt{\frac{G_c}{(\frac{6}{\pi}\mu + \frac{16}{9\pi^2}(\kappa - 2\mu))\delta}}, \tag{22}$$

where G_c denotes the critical energy release rate, and μ and κ represent the shear modulus and bulk modulus, respectively.

If elasto/visco-plastic phenomena exhibit, the critical bond stretch criterion is no longer applicable. To deal with rate-dependent plastic models in the PD framework, Foster and collaborators [18] proposed a failure criterion based on the energy release rate. Subsequently, Madenci and Oterkus [17] presented an alternative energy-based failure criterion for elasto-plastic problems with isotropic hardening. A similar energy-based criterion for shell structures was introduced in Ref. [6]. The critical value for each interaction bond g_c is expressed as

$$g_c = \frac{G_c}{N_c}, \tag{23}$$

where G_c denotes the critical energy release rate. N_c represents the total number of interaction bonds eliminated to create a unit crack surface, with $N_c = 36$ for δ=3Δx [6].

The energy release rate computed from the work done by PD force densities is regarded as a measure to determine the state of interaction bonds. The energy release rate for each interaction bond $\bar{g}_{(k)(j)}$ is defined as

$$\bar{g}_{(k)(j)} = \frac{1}{2\Delta x h}(\omega_{(k)(j)} + \omega_{(j)(k)})V_{(k)}V_{(j)}, \tag{24}$$

where Δx denotes the spacing between material points, and $\omega_{(k)(j)}$ and $\omega_{(j)(k)}$ represent the micro-potentials between points k and j.

From the PD force densities acting on the deformed bond, the micro-potential $\omega_{(k)(j)}$ under the assumption of linear elasticity is yielded as

$$\omega_{(k)(j)} = \frac{1}{2h}(t_{ip(k)(j)}s_{ip(k)(j)} + t_{b(k)(j)}s_{b(k)(j)} + t_{s(k)(j)}s_{s(k)(j)})\xi, \tag{25}$$

in which $s_{s(k)(j)}$=($w_{(j)}$-$w_{(k)}$)/ξ is defined.

The nonlocal interaction is irreversibly terminated between material points to model crack segments when the physical measure reaches its critical value, either for the critical bond stretch or the critical energy density. $\mu_{(k)(j)}$ is introduced into the PD equation of motion to denote the state of each interaction bond; specifically,

$$\mu_{(k)(j)} = \begin{cases} 0 & \text{broken bond,} \\ 1 & \text{intact bond.} \end{cases} \tag{26}$$

3. Arbitrary horizon domain method for PD parameters

In the standard approach to BBPD and OSPD, the PD parameters computed under the complete horizon are kept constant for every material point in the analysis domain. Because the horizon near domain boundaries or crack surfaces is incomplete, these constant PD parameters can not correctly reproduce material behavior (see Fig. 3). Therefore, several numerical corrections have been proposed to reduce the surface effect in BBPD and OSPD. To compensate for the difference in PD force densities near domain boundaries or crack surfaces, the force density is modified by multiplying a correction factor in most surface effect corrections. In contrast to regular surface effect corrections, the variable PD parameters are computed using the actual influence domain of the horizon in the arbitrary horizon domain method. The actual influence domains near discontinuities in the arbitrary horizon domain method are similar to the visibility criterion [32] in the meshfree method (see Fig. 4).

The arbitrary horizon domain method is introduced in this section. By comparing dilatations and SEDs between PD and CCM, the variable PD parameters are obtained. In the derivation of the proposed method, the membrane, bending, and transverse shear deformations are included.

3.1. Membrane deformation

At first, the PD parameters in the membrane term are derived. The displacement components of point j are expressed using Taylor's series expansion as

$$\begin{aligned} u_{(j)} &= u_{(k)} + u_{,x(k)}(x_{(j)} - x_{(k)}) + u_{,y(k)}(y_{(j)} - y_{(k)}), \\ v_{(j)} &= v_{(k)} + v_{,x(k)}(x_{(j)} - x_{(k)}) + v_{,y(k)}(y_{(j)} - y_{(k)}), \end{aligned} \tag{27}$$

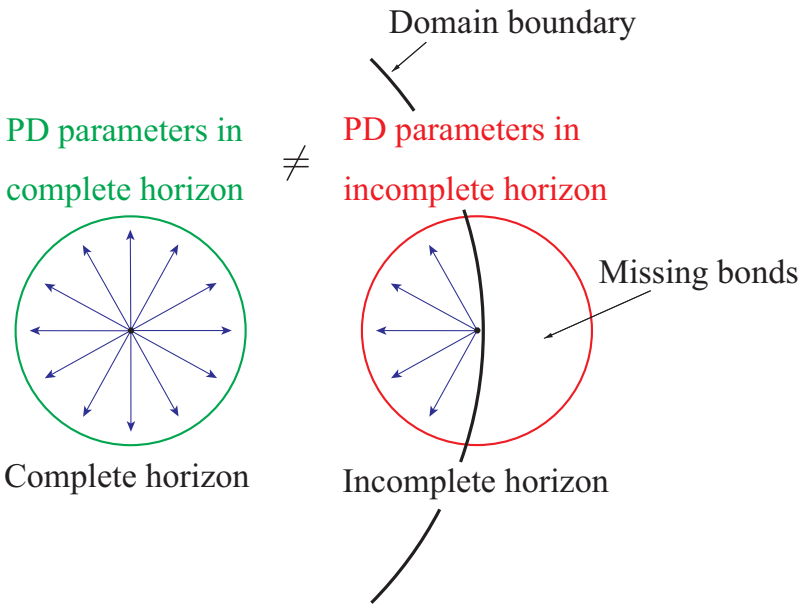

Figure 3: Surface effect in PD caused from PD parameters computation.

which can be rewritten as

$$\begin{aligned} \frac{u_{(j)} - u_{(k)}}{\xi} &= u_{,x(k)} \cos\varphi + u_{,y(k)} \sin\varphi, \\ \frac{v_{(j)} - v_{(k)}}{\xi} &= v_{,x(k)} \cos\varphi + v_{,y(k)} \sin\varphi. \end{aligned} \tag{28}$$

By substituting Eq. (28) into Eq. (4), the bond stretch for the membrane term is expressed as

$$s_{ip(k)(j)} = u_{,x(k)} \cos^2\varphi + u_{,y(k)} \sin\varphi \cos\varphi + v_{,x(k)} \sin\varphi \cos\varphi + v_{,y(k)} \sin^2\varphi. \tag{29}$$

Under the isotropic expansion condition ($u_{,x(k)}$=ζ, $v_{,y(k)}$=ζ), the dilatation of PD in Eq. (6) becomes

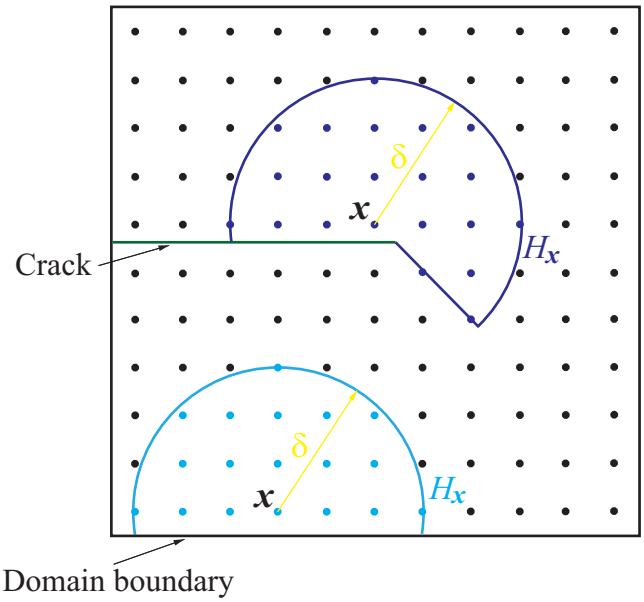

Figure 4: Actual influence domain of the horizon near a domain boundary and a crack surface.

$$\begin{aligned}\vartheta_{ip(k)}^{PD} =& d_{ip}h\int_{H_x}\underline{w}s_{ip(k)(j)}\xi dA\\ =& d_{ip}h\int_{H_x}\underline{w}(\zeta\cos^2\varphi+\zeta\sin^2\varphi)\xi dA\\ =& d_{ip}h\int_{H_x}\underline{w}\zeta\xi dA.\end{aligned}\tag{30}$$

The dilatation of CCM under the isotropic expansion condition becomes

$$\vartheta_{ip(k)}^{CM}=2\zeta.\tag{31}$$

By comparing the dilatation for the membrane term between PD and CCM, the PD parameter d_{ip} is obtained as

$$d_{ip}=\frac{2}{h\int_{H_x}\underline{w}\xi dA}.\tag{32}$$

Similarly, the SED of PD in Eq. (1) under the isotropic expansion condition ($u_{,x(k)}$=ζ, $v_{,y(k)}$=ζ, and $\vartheta_{ip(k)}$=2ζ) becomes

$$\begin{aligned}\bar{W}_{ip}^{PD} =& a_{ip}\vartheta_{ip(k)}^2+b_{ip}h\int_{H_x}\underline{w}s_{ip(k)(j)}^2\xi^2dA\\ =& a_{ip}(2\zeta)^2+b_{ip}h\int_{H_x}\underline{w}\zeta^2\xi^2dA.\end{aligned}\tag{33}$$

The SED of CCM under the isotropic expansion condition becomes

$$\bar{W}_{ip(k)}^{CM}=\frac{Eh}{1-\nu}\zeta^2.\tag{34}$$

By comparing the SED for the membrane term between PD and CCM, the PD parameter a_{ip} is obtained as

$$a_{ip}=\frac{E}{4(1-\nu)}-\frac{b_{ip}h}{4}\int_{H_x}\underline{w}\xi^2dA.\tag{35}$$

Under the simple shear condition ($u_{,y(k)}=\zeta$, $v_{,x(k)}=\zeta$, and $\vartheta_{ip(k)}=0$), the SED of PD in Eq. (1) becomes

$$\begin{aligned}\bar{W}_{ip}^{PD} =& b_{ip}h\int_{H_x}\underline{w}s_{ip(k)(j)}^2\xi^2 dA \\ =& b_{ip}h\int_{H_x}\underline{w}(\zeta\sin\varphi\cos\varphi)^2\xi^2 dA.\end{aligned} \tag{36}$$

The SED of CCM under the simple shear condition becomes

$$\bar{W}_{ip(k)}^{CM} = \frac{Eh}{4(1+\nu)}\zeta^2. \tag{37}$$

In a similar comparison of the SED, the PD parameter b_{ip} is obtained as

$$b_{ip} = \frac{E}{4(1+\nu)}\frac{1}{\int_{H_x}\underline{w}(\xi\cos\varphi\sin\varphi)^2 dA}. \tag{38}$$

3.2. Bending deformation

Next, the PD parameters in the bending term are derived in a similar manner to the computation in the membrane term. By using Taylor series expansion, the rotation components of point j are expressed as

$$\begin{aligned}\theta_{x(j)} &= \theta_{x(k)} + \theta_{x,x(k)}(x_{(j)} - x_{(k)}) + \theta_{x,y(k)}(y_{(j)} - y_{(k)}), \\ \theta_{y(j)} &= \theta_{y(k)} + \theta_{y,x(k)}(x_{(j)} - x_{(k)}) + \theta_{y,y(k)}(y_{(j)} - y_{(k)}),\end{aligned} \tag{39}$$

which can be rewritten as

$$\begin{aligned}\frac{\theta_{x(j)} - \theta_{x(k)}}{\xi} &= \theta_{x,x(k)}\cos\varphi + \theta_{x,y(k)}\sin\varphi, \\ \frac{\theta_{y(j)} - \theta_{y(k)}}{\xi} &= \theta_{y,x(k)}\cos\varphi + \theta_{y,y(k)}\sin\varphi.\end{aligned} \tag{40}$$

By substituting Eq. (40) into Eq. (5), the bond stretch for the bending term is expressed as

$$s_{b(k)(j)} = -\theta_{y,x(k)} \cos^2\varphi - \theta_{y,y(k)} \sin\varphi\cos\varphi + \theta_{x,x(k)} \sin\varphi\cos\varphi + \theta_{x,y(k)} \sin^2\varphi. \tag{41}$$

Under the isotropic rotation condition ($-\theta_{y,x(k)}$=ζ, $\theta_{x,y(k)}$=ζ), the dilatation of PD in Eq. (7) becomes

$$\begin{aligned} \vartheta_{b(k)}^{PD} =& d_b h \int_{H_x} \underline{w} s_{b(k)(j)} \xi dA \\ =& d_b h \int_{H_x} \underline{w} (\zeta \cos^2\varphi + \zeta \sin^2\varphi) \xi dA \\ =& d_b h \int_{H_x} \underline{w} \zeta \xi dA. \end{aligned} \tag{42}$$

The dilatation of CCM under the isotropic rotation condition becomes

$$\vartheta_{b(k)}^{CM} = 2\zeta. \tag{43}$$

By comparing the dilatation for the bending term between PD and CCM, the PD parameter d_b is obtained as

$$d_b = \frac{2}{h \int_{H_x} \underline{w} \xi dA}. \tag{44}$$

Similarly, the SED of PD in Eq. (2) under the isotropic rotation condition ($-\theta_{y,x(k)}$=ζ, $\theta_{x,y(k)}$=ζ, and $\vartheta_{b(k)}$=2ζ) becomes

$$\begin{aligned} \bar{W}_b^{PD} =& a_b \vartheta_{b(k)}^2 + b_b h \int_{H_x} \underline{w} s_{b(k)(j)}^2 \xi^2 dA \\ =& a_b (2\zeta)^2 + b_b h \int_{H_x} \underline{w} \zeta^2 \xi^2 dA. \end{aligned} \tag{45}$$

The SED of CCM under the isotropic rotation condition becomes

$$\bar{W}_{b(k)}^{CM} = \frac{E h^3}{12(1-\nu)} \zeta^2. \tag{46}$$

By comparing the SED for the bending term between PD and CCM, the PD parameter a_b is obtained as

$$a_b = \frac{Eh^3}{48(1-\nu)} - \frac{b_b h}{4}\int_{H_x} \underline{w}\xi^2 dA. \tag{47}$$

Under the torsion condition ($-\theta_{y,y(k)}=\zeta$, $\theta_{x,x(k)}=\zeta$, and $\vartheta_{b(k)}=0$), the SED of PD in Eq. (2) becomes

$$\begin{aligned}\bar{W}_b^{PD} =& b_b h \int_{H_x} \underline{w} s_{b(k)(j)}^2 \xi^2 dA \\ =& b_b h \int_{H_x} \underline{w}(\zeta \sin\varphi \cos\varphi)^2 \xi^2 dA.\end{aligned} \tag{48}$$

The SED of CCM under the torsion condition becomes

$$\bar{W}_{b(k)}^{CM} = \frac{Eh^3}{48(1+\nu)}\zeta^2. \tag{49}$$

In a similar comparison of the SED, the PD parameter b_b is obtained as

$$b_b = \frac{Eh^2}{48(1+\nu)} \frac{1}{\int_{H_x} \underline{w}(\xi \cos\varphi \sin\varphi)^2 dA}. \tag{50}$$

3.3. Transverse shear deformation

Finally, the PD parameter in the transverse shear term is derived. The transverse deflection component of point j is expressed using Taylor's series expansion as

$$w_{(j)} = w_{(k)} + w_{,x(k)}(x_{(j)} - x_{(k)}) + w_{,y(k)}(y_{(j)} - y_{(k)}), \tag{51}$$

which can be rewritten as

$$\frac{w_{(j)} - w_{(k)}}{\xi} = w_{,x(k)} \cos\varphi + w_{,y(k)} \sin\varphi. \tag{52}$$

By substituting Eq. (52) into Eq. (3) and assuming $\bar{\theta}_{(k)}$=$\bar{\theta}_{(j)}$, the SED of PD under the transverse shear condition ($(w_{,x}+\theta_y)=\zeta$, $(w_{,y}-\theta_x)=\zeta$) becomes

$$\begin{aligned}
\bar{W}_s^{PD} =& \frac{1}{4}C_s h \int_{H_x} \underline{w}(\frac{w_{(j)}-w_{(k)}}{\xi} - \bar{\theta}_{(k)})^2 \xi^2 dA \\
=& \frac{1}{4}C_s h \int_{H_x} \underline{w}[(w_{,x}+\theta_y)\cos\varphi + (w_{,y}-\theta_x)\sin\varphi]^2 \xi^2 dA \\
=& \frac{1}{4}C_s h \int_{H_x} \underline{w}(\zeta^2\cos^2\varphi + \zeta^2\sin^2\varphi)\xi^2 dA \\
=& \frac{1}{4}C_s h \int_{H_x} \underline{w}\zeta^2\xi^2 dA.
\end{aligned} \tag{53}$$

The SED of CCM under the transverse shear condition becomes

$$\bar{W}_s^{CM} = \frac{k_s E h}{2(1+\nu)}\zeta^2. \tag{54}$$

By comparing the SED for the transverse shear term between PD and CCM, the PD parameter C_s is obtained as

$$C_s = \frac{k_s E}{1+\nu}\frac{2}{\int_{H_x}\underline{w}\xi^2 dA}. \tag{55}$$

For the proposed method, the PD parameters integrated over the complete circle horizon are the same as those given in the standard approach [6]. It confirms that the PD parameters are correctly derived in the arbitrary horizon domain method. In the computational procedure, the PD parameters are numerically integrated by summing the integrand over the horizon. The volume correction is thereby also adopted in the numerical integration of PD parameters.

4. Numerical examples

The OSPD shell model incorporated with the arbitrary horizon domain method is employed in the present study. Four numerical examples of shell structures are considered to examine fracture mechanics behaviors under in-plane or out-of-plane loading. CODs and SEDs corresponding to the critical

bond stretch and critical energy density criteria, respectively, are regarded as the assessed objectives. Additionally, a crack propagation analysis is also performed using the proposed method. A uniform particle distribution is employed, and the horizon size δ is set to $3.015\Delta x$ [31]; here, Δx denotes the particle spacing.

Three PD approaches are considered in the present study. Those approaches are labeled " Approach 1 " for the standard method without correction, " Approach 2 " for the volume method, and " Approach 3 " for the arbitrary horizon domain method. The volume correction mentioned in Eq. (21) is adopted in all three approaches. A commercial FEM software, ABAQUS [34], is used to compute reference results with linear elastic fracture mechanics settings. The element size of the FEM models near the crack tip is set to approximately 0.001 m.

4.1. 2D plane stress problem for the near-tip solution with a stationary crack under Mode-I fracture

An infinite plate with a central crack under biaxial tensile load is analyzed. To simplify this example, a 2D plane stress model under specified displacement boundary conditions (BCs) is considered to examine the near-tip solutions in linear elastic fracture mechanics. The length L and width W are 1 m, and the crack length a is 0.5 m. Young's modulus E and Poisson's ratio ν are set to 1 GPa and 0.25, respectively. The analytical solutions for the near-tip displacement and stress fields [33] are expressed in the form

$$\begin{bmatrix} u \\ v \end{bmatrix} = \frac{K_I}{2\mu}\sqrt{\frac{r'}{2\pi}} \begin{bmatrix} \cos\frac{\theta'}{2}(\kappa - 1 + 2\sin^2\frac{\theta'}{2}) \\ \sin\frac{\theta'}{2}(\kappa + 1 - 2\cos^2\frac{\theta'}{2}) \end{bmatrix}, \tag{56}$$

$$\begin{bmatrix} \sigma_{xx} \\ \sigma_{yy} \\ \tau_{xy} \end{bmatrix} = \frac{K_I}{\sqrt{2\pi r}} \begin{bmatrix} \cos\frac{\theta'}{2}(1 - \sin\frac{\theta'}{2}\sin\frac{3\theta'}{2}) \\ \cos\frac{\theta'}{2}(1 + \sin\frac{\theta'}{2}\sin\frac{3\theta'}{2}) \\ \cos\frac{\theta'}{2}\sin\frac{\theta'}{2}\cos\frac{3\theta'}{2} \end{bmatrix}, \tag{57}$$

where μ=E/2(1+ν) and κ=(3-ν)/(1+ν). K_I=1.0 MPa$\sqrt{\text{mm}}$ is set. The origin of the polar coordinate system (r',θ') is placed at the crack tip. The specified displacement BCs given in Eq. (56) are applied (see Fig. 5). Three different particle spacings are used, specifically, Δx=1/80, 1/160, and 1/320 m.

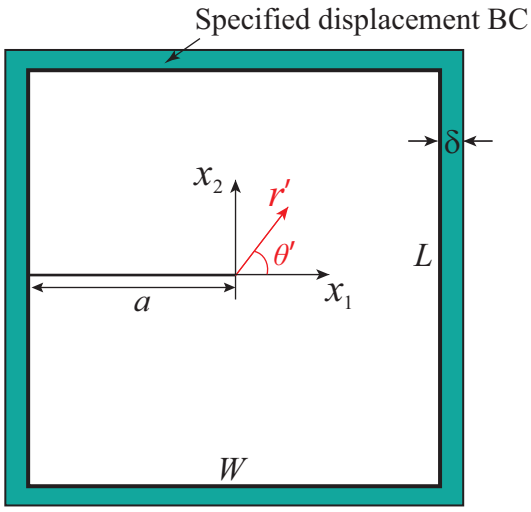

Figure 5: 2D plane stress model under specified displacement BCs with a stationary crack.

A convergence analysis of the displacement fields is performed. The L2-norm in Eq. (58) is selected to estimate the error by comparing the PD results with the analytical solution. The rates of convergence for the entire domain and the crack surface are presented in Fig. 6(a) and (b), respectively. Approach 1 produces slower convergence rates in both circumstances. Similar convergence rates in Fig. 6(a) are found for Approaches 2 and 3. In Fig. 6(b), however, Approach 3 has a better convergence rate than Approach 2.

$$error = \sqrt{\int_{\Omega} (u^{PD} - u^{Ref})^2 d\Omega}, \tag{58}$$

where u^{PD} and u^{Ref} are the displacement results from the PD and reference solutions, respectively.

The COD results, u_y, obtained from the analytical solution and Approach 3 are compared along the crack surface (see Fig. 7(a)). Both sets of results are in good agreement with each other. Furthermore, the SED along the crack surface and crack front is investigated. The SED results of the analytical solution and three PD approaches are illustrated in Fig. 7(b). The SED results of Approach 3 are found to be most similar to those of the analytical solution. Moreover, the arbitrary horizon domain method is able to evaluate

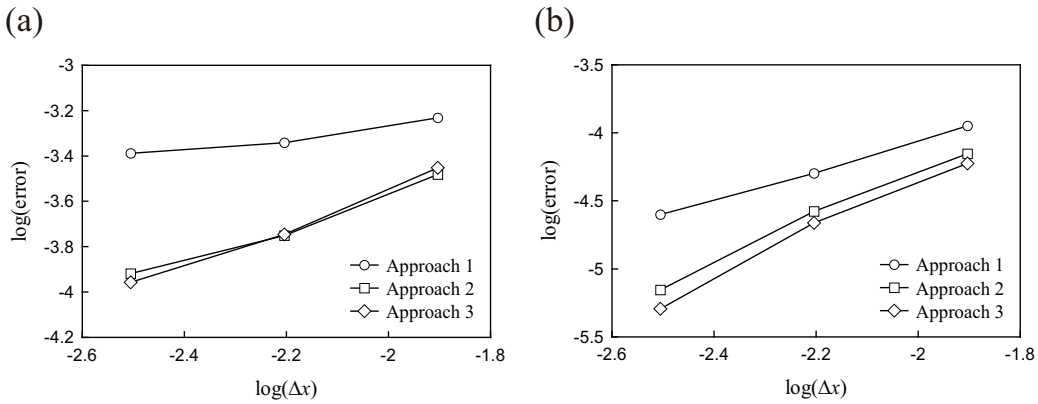

Figure 6: Convergence analysis of the displacement fields, (a) Entire domain, (b) Crack surface.

the SED in linear elastic fracture mechanics. Even near the crack tip, the proposed method provides a reasonable SED solution.

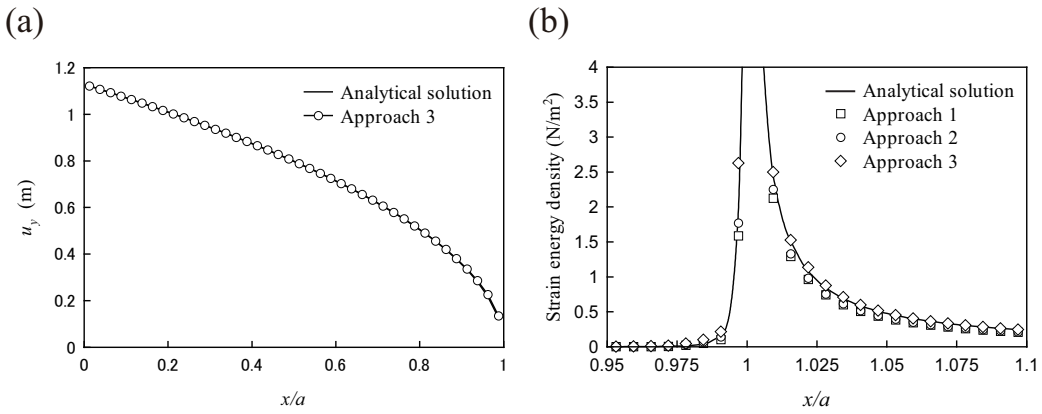

Figure 7: Fracture mechanics quantities, (a) Displacement u_y, (b) Strain energy density.

4.2. Rectangular shell with an inclined edge crack under tensile load

A rectangular shell with an inclined edge crack under tensile load is calculated. The length L, width W, and thickness h of the rectangular shell are 1 m, 0.5 m, and 0.1 m, respectively. The crack length a is 0.2 m, and

the crack angle β is 45°. A uniform tensile stress of σ=1.0 MPa is applied on the top edge, and displacement BCs are adopted on the bottom edge (see Fig. 8). Young's modulus E and Poisson's ratio ν are set to 200 GPa and 0.3, respectively. A particle spacing of Δx=1/320 m is used.

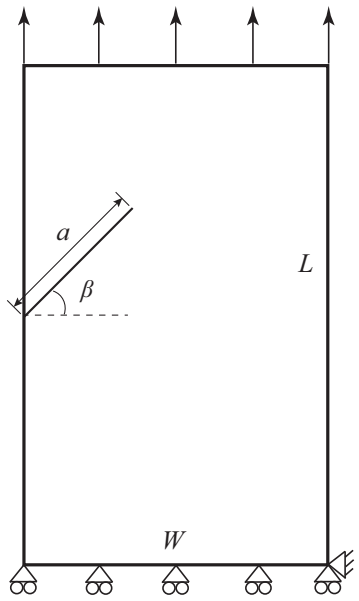

Figure 8: Rectangular shell under tensile load with an inclined edge crack.

The COD results, u_y, along the inclined crack surface are presented in Fig. 9(a). Approach 3 appears to match well with the FEM solution than the other two approaches. The deformation contours, u_y, from Approach 3 and FEM are given in Fig. 10. From linear elastic fracture mechanics, the stresses tend to infinity near the crack tip. Because of the stress singularity, the near-tip stress fields can not be determined from FEM simulations. Therefore, a comparison of the SED results is plotted (see Fig. 9(b)) from x'/a=1.1 along the crack front; here, x' denotes the x-axis of the local Cartesian coordinate system. From this comparison, the SED results of Approach 1 show an obvious difference from those of Approaches 2 and 3. After further discussion, the SED results of Approach 2 are slightly lower than those of the FEM solution, and Approach 3 provides the closest SED results to the FEM solution. It indicates that the arbitrary horizon domain method well assesses COD and SED for mixed-mode fracture problems.

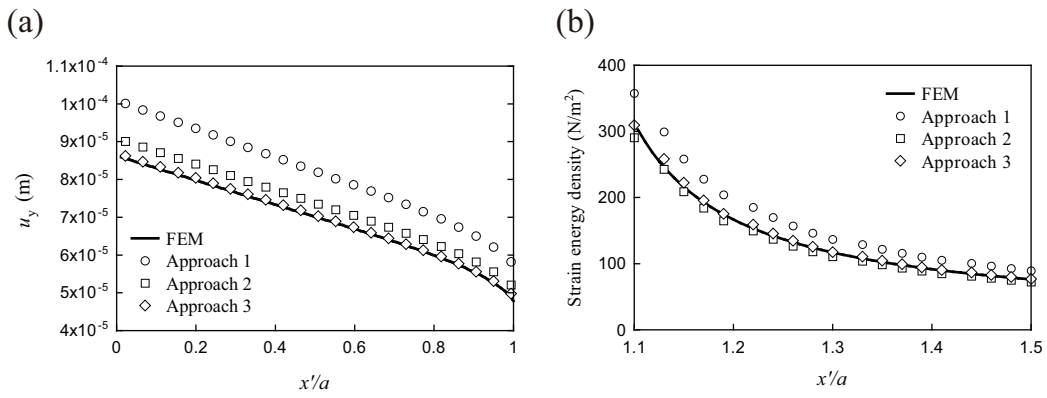

Figure 9: Fracture mechanics quantities, (a) Displacement u_y, (b) Membrane strain energy density.

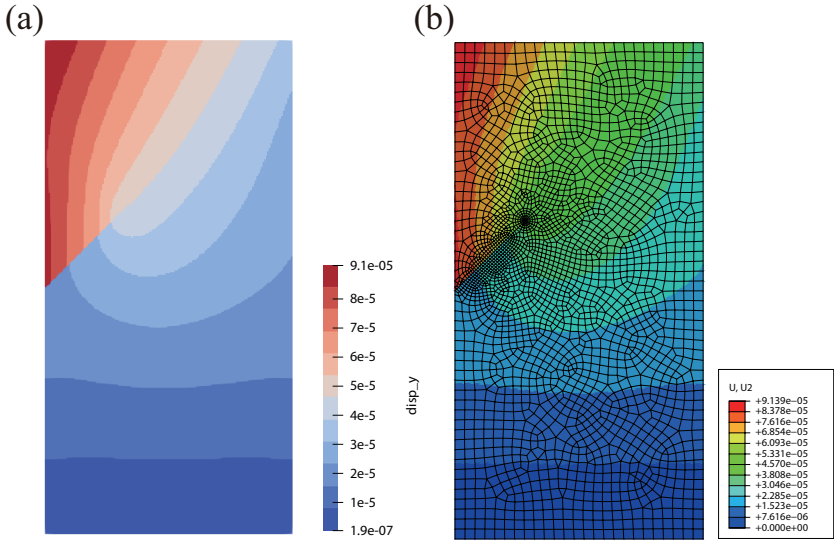

Figure 10: u_y deformation contours, (a) Approach 3, (b) FEM.

4.3. Square shell with a central crack under uniform pressure

A square shell with a central crack under uniform pressure is investigated. The length L, width W, and thickness h of the square shell are 1 m, 1 m, and 0.1 m, respectively. The half crack length a is 0.1 m. The shell is subjected to a uniform pressure of p_0=1.0 MPa in the transverse direction with clamped BCs imposed on all the edges (see Fig. 11). Young's modulus E and Poisson's ratio ν are set to 200 GPa and 0.3, respectively. A particle spacing of Δx=1/320 m is used.

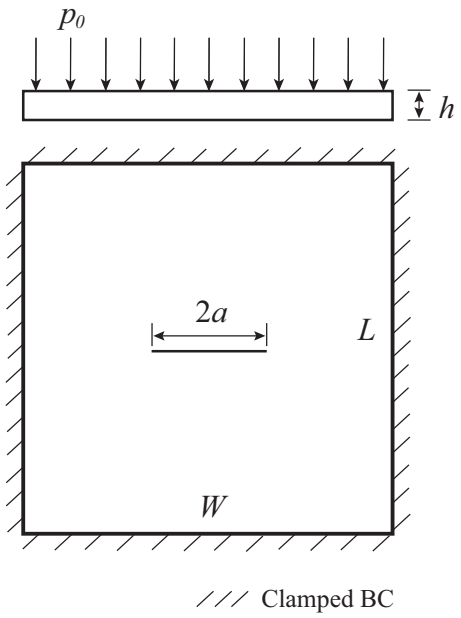

Figure 11: Square shell under uniform pressure with a central crack.

The COD results, including u_z, θ_x, and θ_y, along the crack surface are shown in Fig. 12(a), (b), and (c), respectively. The COD results are improved under Approach 3 to obtain the most similar results to the FEM solution for not only transverse deformation but also rotation deformations. The deformation contours, θ_x, from Approach 3 and FEM are presented in Fig. 13. The SED of the bending term dominates in the example instead of the transverse shear term. Therefore, only the SED of the bending term illustrated in Fig. 12(d) is discussed. The SED results of both Approaches 2 and 3 agree well with those of the FEM solution. In general, accurate

results for CODs and SED under out-of-plane loading can be obtained from the arbitrary horizon domain method.

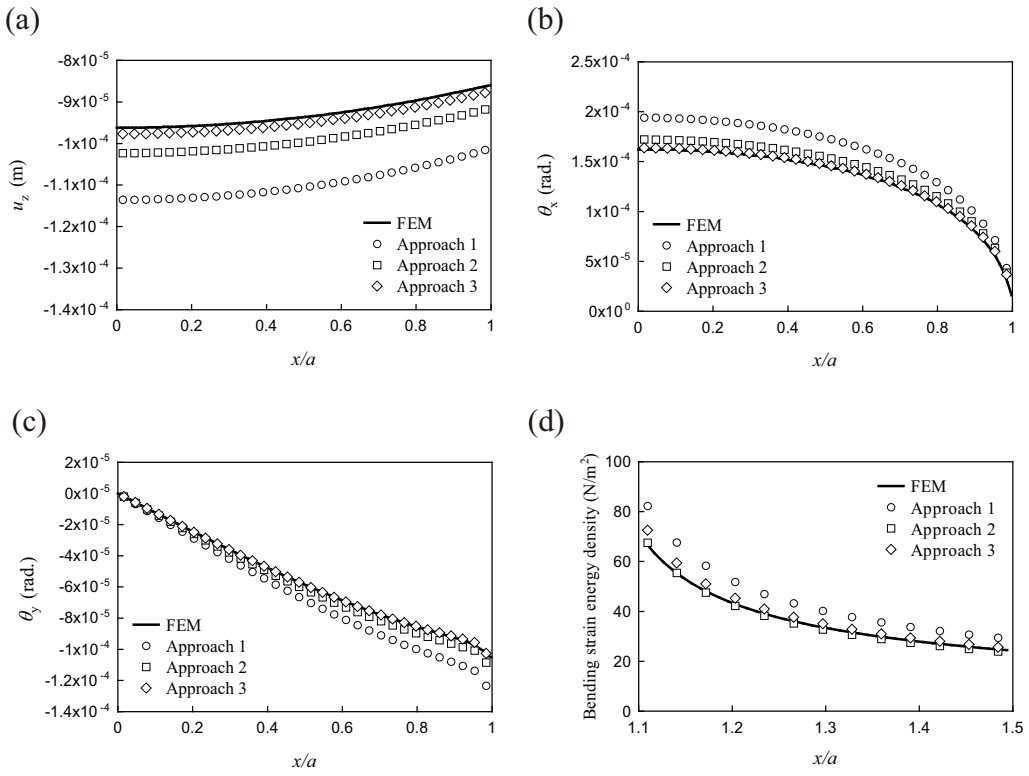

Figure 12: Fracture mechanics quantities, (a) Displacement u_z, (b) Rotation θ_x, (c) Rotation θ_y, (d) Bending strain energy density.

4.4. Rectangular shell with an inclined central crack under bending load

A rectangular shell with an inclined central crack under bending load is simulated. The length L, width W, and thickness h of the rectangular shell are 0.5 m, 1 m, and 0.1 m, respectively. The half crack length a is 0.1 m, and the crack angle β is 45°. The rectangular shell is subjected to bending moments of M=10.0 kPa-m with simply supported BCs on the right and left edges (see Fig. 14). Young's modulus E and Poisson's ratio ν are set to 200 GPa and 0.3, respectively. A particle spacing of Δx=1/320 m is used.

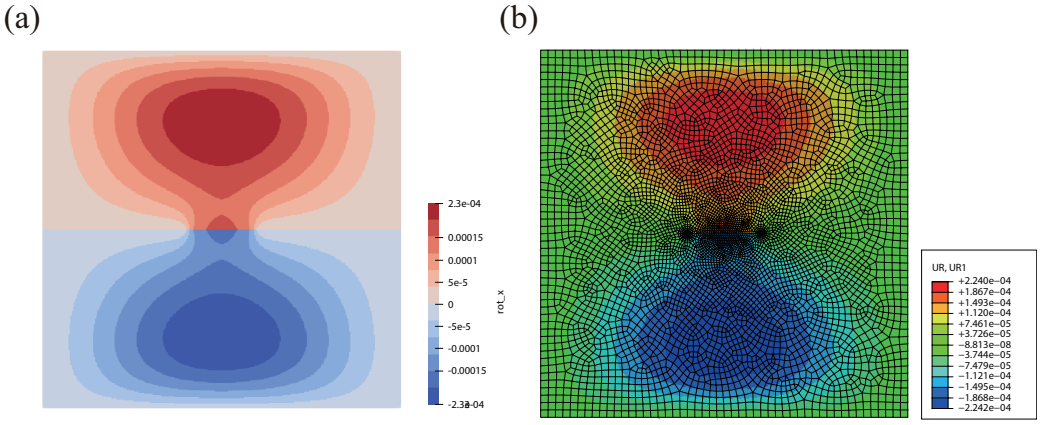

Figure 13: θ_x deformation contours, (a) Approach 3, (b) FEM.

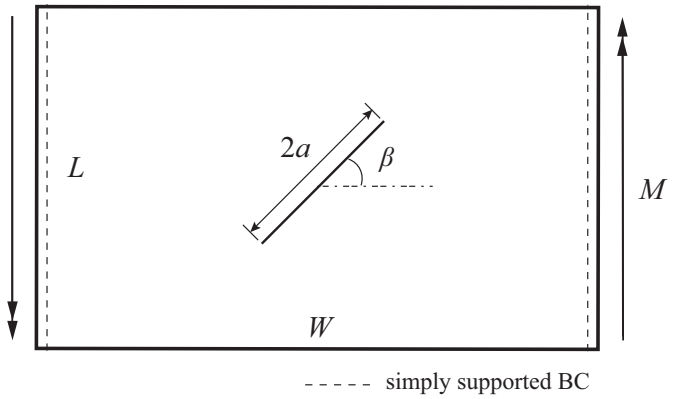

Figure 14: Rectangular shell under bending load with an inclined central crack.

The COD results for u_z, θ_x, and θ_y along the inclined crack surface are presented in Fig. 15(a), (b), and-(c), respectively. As for the third example, the results for the transverse and rotation deformations from Approach 3 are most similar to those from the FEM solution. The deformation contours, θ_y, from Approach 3 and FEM are drawn in Fig. 16. Likewise, a comparison of the SED results of the bending term along the crack front from x'/a=1.1 is plotted in Fig. 15(d). In contrast to Approach 1, Approaches 2 and 3 distinctly provide better SED results. In a detailed comparison between Approaches 2 and 3, the SED results of Approach 3 are closest to those of the FEM solution. In other words, CODs and SED in mixed-mode fracture problems involving out-of-plane loading are well reproduced using the arbitrary horizon domain method.

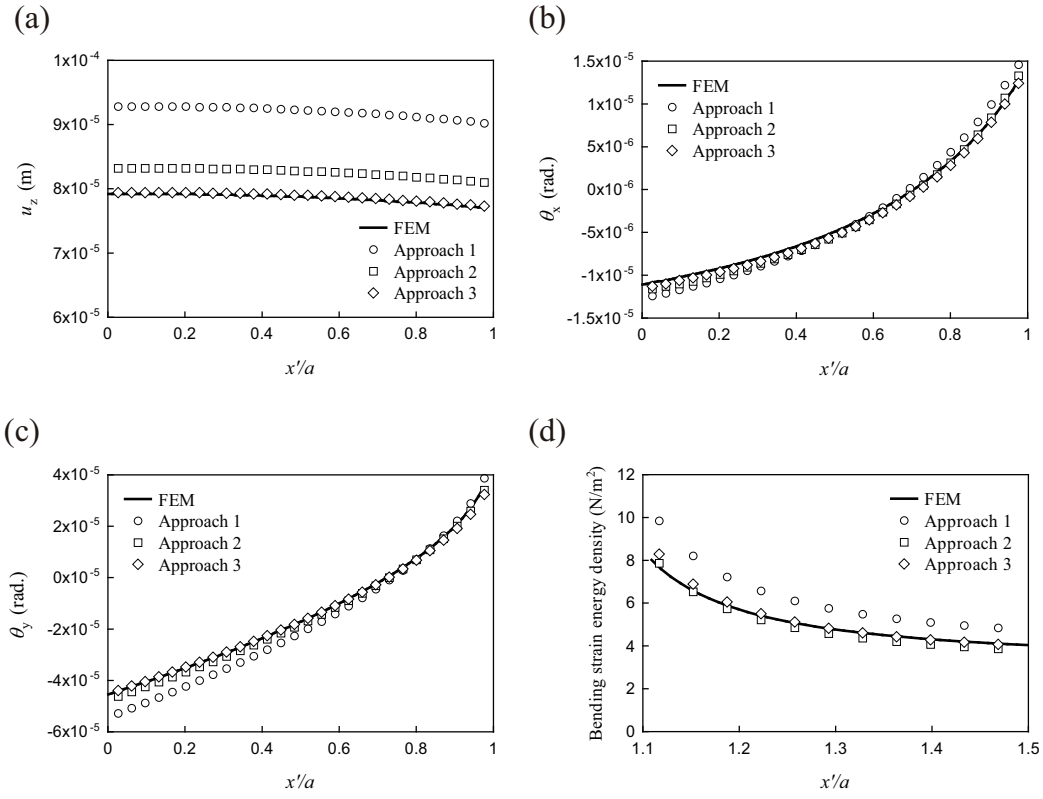

Figure 15: Fracture mechanics quantities, (a) Displacement u_z, (b) Rotation θ_x, (c) Rotation θ_y, (d) Bending strain energy density.

(a)

(b)

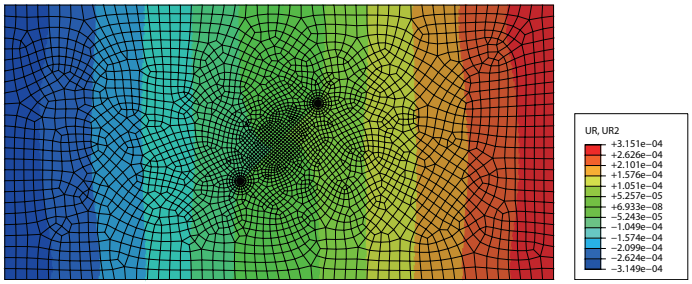

Figure 16: θ_y deformation contours, (a) Approach 3, (b) FEM.

4.5. Diagonally loaded square plate with a central pre-existing crack

A crack propagation analysis of the DLSP specimen [30] with an inclined central crack is performed. The geometrical dimension $2W$ and plate thickness h are 0.15 m and 0.005 m, respectively. The initial half crack length a is set to 0.045, and the crack orientation β is set to one of five different angles, specifically, 0°, 15°, 30°, 45°, and 62.5°. Young's modulus E=2.94 GPa, Poisson's ratio ν=0.38, and density ρ=1,200 kg/m^3 are chosen. A constant displacement increment of Δu=2.5$\times$ 10^{-7} m [35] is applied within the circle holes at the top and bottom corners. The radius of each circle hole is 0.004 m, and the distance q between the center of each circle hole and the plate corner is 0.025 m. The DLSP model is sketched in Fig. 17. A particle spacing of Δx=0.001 m is used. The fracture toughness of the material K_c is set to 1.33 MPa$\sqrt{\text{m}}$, and its critical energy release rate G_c is set to 601.667 N/m. The critical bond stretch s_c obtained from Eq. (22) is 9.145$\times$ 10^{-3}.

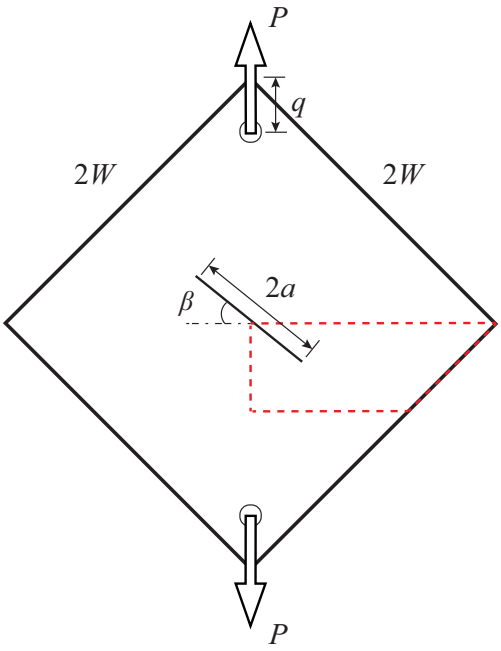

Figure 17: Diagonally loaded square plate with a central pre-existing crack.

From the numerical examples simulated above, CODs are well evaluated near the crack tip under single- and mixed-mode fracture conditions. On the

other hand, SEDs can not be properly predicted near the crack tip owing to the stress singularity. The material of the DLSP specimen is a brittle polymer called polymethyl methacrylate (PMMA). Therefore, the critical bond stretch criterion, which is suited for brittle materials, is adopted. Additionally, Approach 3 is employed in this crack propagation analysis.

The crack propagation paths for different crack orientations obtained from PD and experiment [30] are presented in Fig. 18. To examine the crack paths in detail, crack path comparisons with initial crack orientations 15° to 62.5° within the region marked by red dashed lines in the model are shown in Fig. 19. The reference solutions from experiment and extended FEM [36] are selected. From the comparisons, the crack paths are well predicted for all crack orientations when using the arbitrary horizon domain method. Moreover, the initial crack growth angle for different crack orientations is investigated in a comparison of PD and experiment. As expressed in Fig. 20, the PD results are in good agreement with those from experimental data.

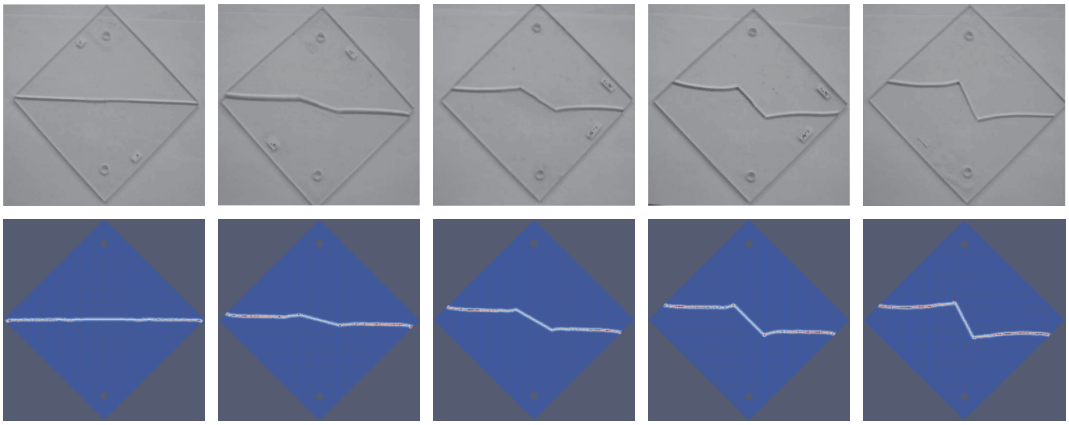

Figure 18: Crack propagation paths from experiment [30] (upper) and PD (lower).

5. Conclusion

The OSPD shell model is introduced to evaluate fracture mechanics behaviors of thin-walled structures. In the standard PD framework, the constant PD parameters for each material point are derived based on the complete horizon. The surface effect takes place because the constant PD parameters can not properly reproduce material behavior near domain boundaries

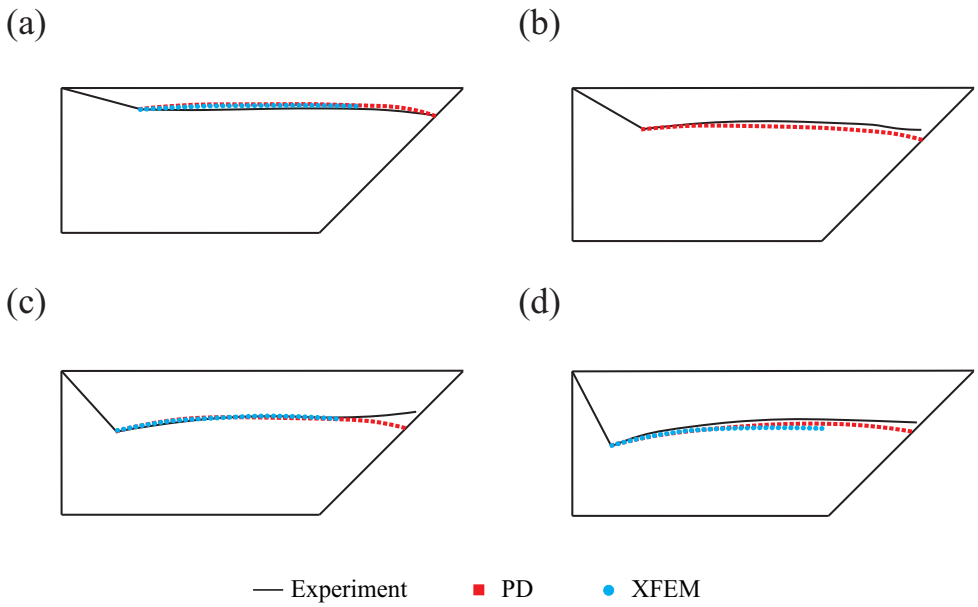

Figure 19: Detailed comparison of crack propagation paths between experiment, PD, and extended FEM [36].

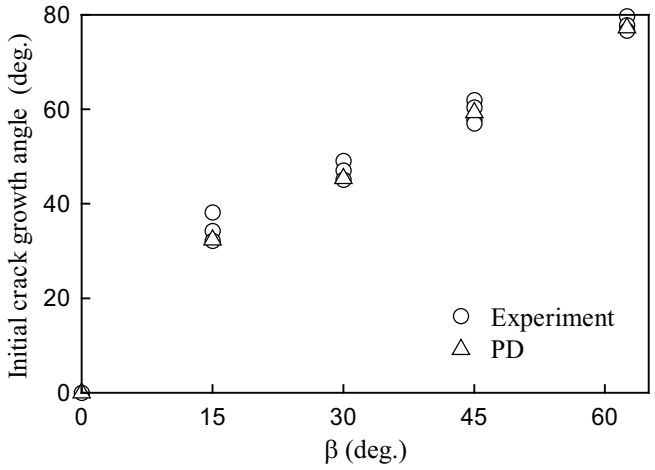

Figure 20: Initial crack growth angles from experiment and PD.

or crack surfaces. It significantly affects the accuracy of computational results, especially near the crack tip. The arbitrary horizon domain method is adopted to minimize the PD surface effect by eliminating the complete horizon assumption. In the previous studies, only two-dimensional plane problems have been considered using similar approaches with arbitrary horizon domains. Here, the arbitrary horizon domain method is incorporated into the OSPD shell model involving the membrane, bending, and transverse shear deformations. Moreover, the volume correction and adaptive dynamic relaxation techniques are employed in the proposed method.

Several numerical examples, including single- and mixed-mode fracture problems, are considered to examine CODs and SEDs under in-plane or out-of-plane loading. The COD and SED results obtained from three different PD approaches are compared with those from the FEM simulations. The volume method and the arbitrary horizon domain method provide effective approaches to reduce the influence from the PD surface effect. The actual volume of the horizon for each material point in the analysis domain is considered in both methods. However, the volume method assumes that each interaction bond within the horizon equally contributes to the PD force density. Thus, the PD force density is approximated by merely multiplying a ratio of the complete volume to the present volumes. In contrast to the volume method, as expounded in Section 3, the PD parameters in the arbitrary horizon domain method are a function of distance and angle between material points. For the PD force density, each interaction bond within the horizon no longer contributes equally. The arbitrary horizon domain method can precisely simulate physical behavior near domain boundaries or crack surfaces. From the comparisons of CODs and SEDs presented in Section 4, the arbitrary horizon domain method provides good agreement with the FEM solution than the other two approaches. Moreover, the proposed method is applied to predict crack paths in the crack propagation analysis of the DLSP specimen. These predictions for different crack orientations well match the experimental data.

Appendix A. Examination of varied plate thickness

To verify the capability of the arbitrary horizon domain method for shells with different thicknesses, the same example discussed in Section 4.3 is investigated. A shell with L/h=10 is considered in Section 4.3. Here, two

additional cases with L/h=5 and 15 are configured to examine CODs in a comparison with the FEM solution.

The COD results for L/h=5 and 15, including u_z, θ_x, and θ_y, are illustrated in Figs. A.1 and A.2, respectively. As the same as the conclusions in Section 4.3, the COD results evaluated from Approach 3 are closest to the FEM solution than the other two approaches. It indicates that the arbitrary horizon domain method can effectively reduce the PD surface effect for shell structures with different thicknesses.

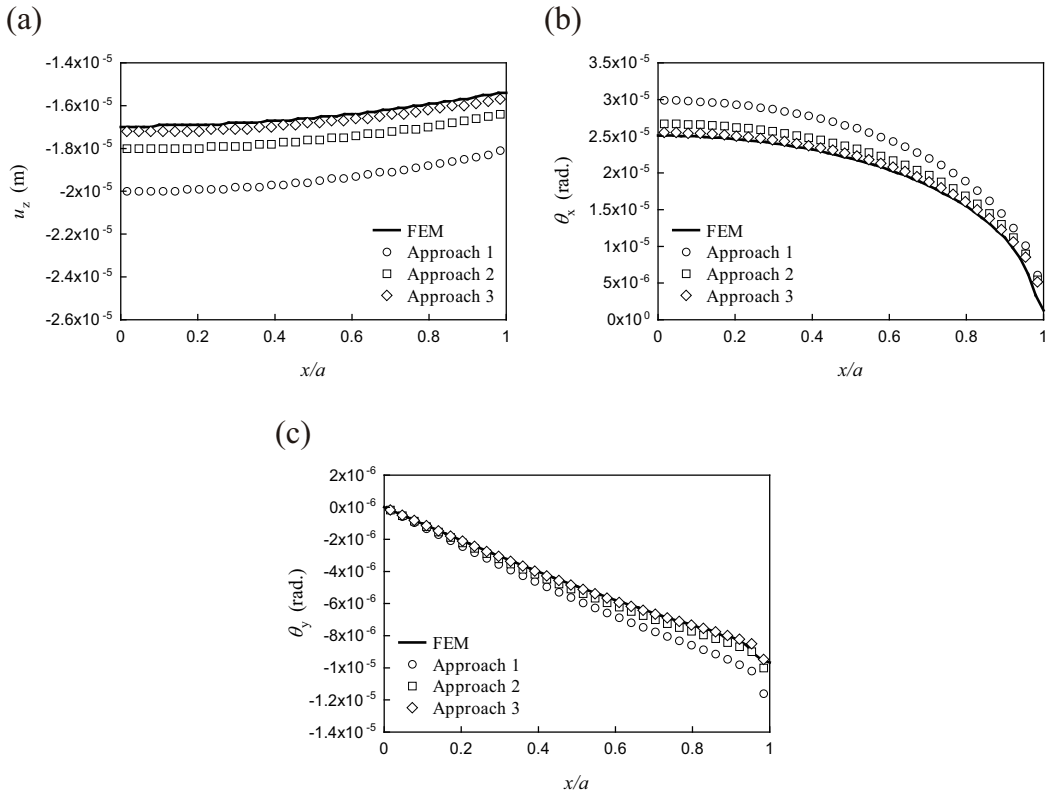

Figure A.1: Fracture mechanics quantities for L/h=5, (a) Displacement u_z, (b) Rotation θ_x, (c) Rotation θ_y.

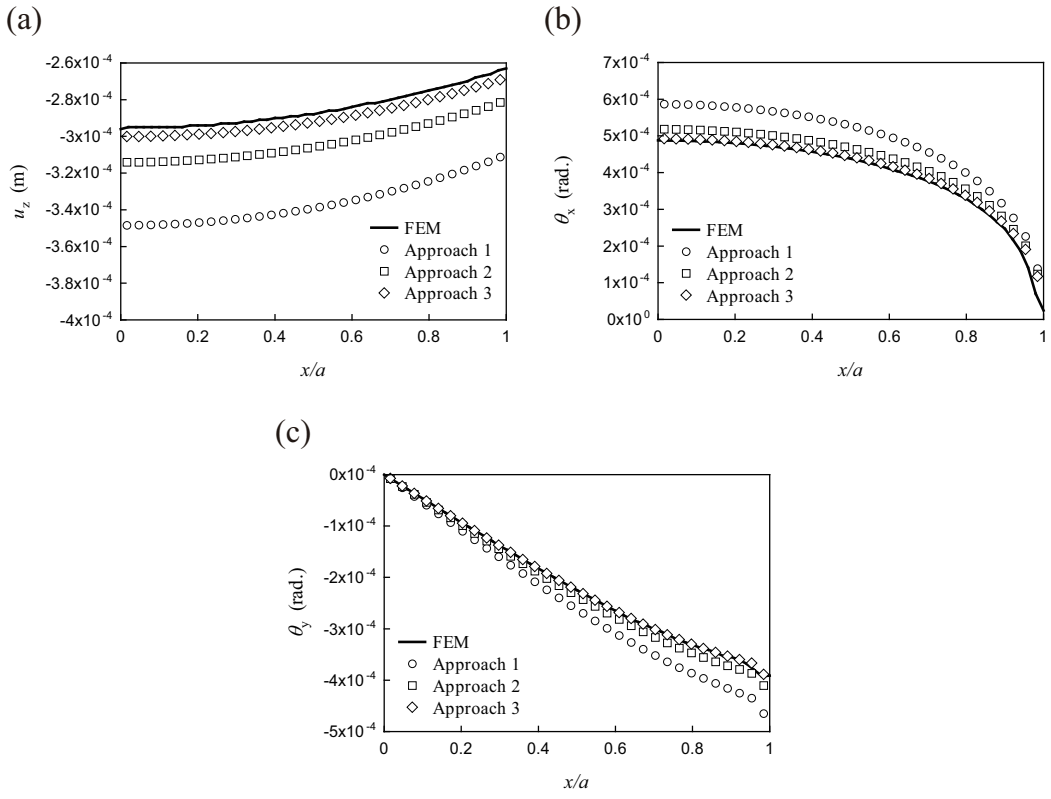

Figure A.2: Fracture mechanics quantities for L/h=15, (a) Displacement u_z, (b) Rotation θ_x, (c) Rotation θ_y.

Acknowledgements

This work was financially supported by Japan-Taiwan Exchange Association. The authors gratefully acknowledge suggestions for this study from Mr. Kuan-Chia Chen.

References

[1] S.A. Silling, Reformulation of elasticity theory for discontinuities and long-range forces, J. Mech. Phys. Solids 48 (2000) 175-209.

[2] S.A. Silling, M. Epton, O. Weckner, J. Xu, E. Askari, Peridynamic states and constitutive modeling, J. Elast. 88 (2007) 151-184.

[3] J. O'Grady, J. Foster, Peridynamic plates and flat shells: A non-ordinary, state-based model, Int. J. Solids Struct. 51 (2014) 4572-4579.

[4] Z. Yang, B. Vazic, C. Diyaroglu, E. Oterkus, S. Oterkus, A Kirchhoff plate formulation in a state-based peridynamic framework, Math. Mech. Solids 25 (2020) 727-738.

[5] C. Diyaroglu, E. Oterkus, S. Oterkus, E. Madenci, Peridynamics for bending of beams and plates with transverse shear deformation, Int. J. Solids Struct. 69 (2015) 152-168.

[6] C.T. Nguyen, S. Oterkus, Peridynamics for the thermomechanical behavior of shell structures, Eng. Fract. Mech. 219 (2019) 106623.

[7] S.R. Chowdhury, P. Roy, D. Roy, J.N. Reddy, A peridynamic theory for linear elastic shells, Int. J. Solids Struct. 84 (2016) 110-132.

[8] J. Heo, Z. Yang, W. Xia, S. Oterkus, E. Oterkus, Buckling analysis of cracked plates using peridynamics, Ocean Eng. 214 (2020) 107817.

[9] J. Heo, Z. Yang, W. Xia, S. Oterkus, E. Oterkus, Free vibration analysis of cracked plates using peridynamics, Ships Offshore Struct. 15 (2020) 220-229.

[10] M.J. Dai, S. Tanaka, S. Oterkus, E. Oterkus, Mixed-mode stress intensity factors evaluation of flat shells under in-plane loading employing ordinary state-based peridynamics, Theor. Appl. Fract. Mech. 112 (2020) 102841.

[11] M.J. Dai, S. Tanaka, T.Q. Bui, S. Oterkus, E. Oterkus, Fracture parameter analysis of flat shells under out-of-plane loading using ordinary state-based peridynamics, Eng. Fract. Mech. 244 (2021) 107560.

[12] M. Dorduncu, Peridynamic modeling of delaminations in laminated composite beams using refined zigzag theory, Theor. Appl. Fract. Mech. 112 (2021) 102832.

[13] M. Dorduncu, K. Kaya, O.F. Ergin, Peridynamic Analysis of Laminated Composite Plates Based on First-Order Shear Deformation Theory, Int. J. Appl. Mech. 12 (2020) 2050031.

[14] C.T. Nguyen, S. Oterkus, Investigating the effect of brittle crack propagation on the strength of ship structures by using peridynamics, Ocean Eng. 209 (2020) 107472.

[15] C.T. Nguyen, S. Oterkus, Ordinary state-based peridynamics for geometrically nonlinear analysis of plates, Theor. Appl. Fract. Mech. 112 (2021) 102877.

[16] S.A. Silling, E. Askari, A meshfree method based on the peridynamic model of solid mechanics, Comput. Struct. 83 (2005) 1526-1535.

[17] E. Madenci, S. Oterkus, Ordinary state-based peridynamics for plastic deformation according to von mises yield criteria with isotropic hardening, J. Mech. Phys. Solids 86 (2016) 192-219.

[18] J.T. Foster, S.A. Silling, W. Chen, An energy based failure criterion for use with peridynamic states, J. Multiscale Comput. Eng. 9 (2011) 675-687.

[19] D. Dipasquale, G. Sarego, M. Zaccariotto, U. Galvanetto, A discussion on failure criteria for ordinary state-based peridynamics, Eng. Fract. Mech. 186 (2017) 378-398.

[20] J. Zhao, H. Tang, S. Xue, A new fracture criterion for peridynamic and dual-horizon peridynamics, Front. Struct. Civ. Eng. 12 (2018) 629-641.

[21] H. Yu, S. Li, On energy release rates in peridynamics, J. Mech. Phys. Solids 142 (2020) 104024.

[22] T.L. Warren, S.A. Silling, A. Askari, O. Weckner, M.A. Epton, J. Xu, A non-ordinary state-based peridynamic method to model solid material deformation and fracture, Int. J. Solids Struct. 46 (2009) 1186-1195.

[23] M. Tupek, J. Rimoli, R. Radovitzky, An approach for incorporating classical continuum damage models in state-based peridynamics, Comput. Methods Appl. Mech. Eng. 263 (2013) 20-26.

[24] Q.V. Le, F. Bobaru, Surface corrections for peridynamic models in elasticity and fracture, Comput. Mech. 61 (2018) 499-518.

[25] S. Oterkus, E. Madenci, A. Agwai, Peridynamic thermal diffusion, J. Comput. Phys. 265 (2014) 71-96.

[26] A.F. Queiruga, G. Moridis, Numerical experiments on the convergence properties of state-based peridynamic laws and influence functions in two-dimensional problems, Comput. Methods Appl. Mech. Eng. 322 (2017) 97-122.

[27] K.C. Chen, The development of coupled peridynamics and isogeometric analysis method for modeling of crack propagation on ship-hull panels (Master thesis), National Taiwan Ocean University, Taiwan, 2020. (in Chinese)

[28] E. Madenci, M. Dorduncu, A. Barut, N. Phan, A state-based peridynamic analysis in afinite element framework, Eng. Fract. Mech. 195 (2018) 104-128.

[29] E. Madenci, M. Dorduncu, A. Barut, N. Phan, Weak form of peridynamics for nonlocal essential and natural boundary conditions, Comput. Methods Appl. Mech. Eng. 337 (2018) 598-631.

[30] M.R. Ayatollahi, M.R.M. Aliha, Analysis of a new specimen for mixed mode fracture tests on brittle materials, Eng. Fract. Mech. 76 (2009) 1563-1573.

[31] E. Madenci, E. Oterkus, Peridynamic theory and its applications, Springer, New York, 2014.

[32] T. Belytschko, Y.Y. Lu, L. Gu, Element-free Galerkin methods, Int. J. Numer. Methods Eng. 37 (1994) 229-256.

[33] T.L. Anderson, Fracture mechanics: fundamentals and applications, CRC Press, Boca Raton, 2004.

[34] H. Hibbitt, B. Karlsson, P. Sorensen, Abaqus analysis user's manual version 6.10, Dassault Systemes Simulia Corp, Providence, 2011.

[35] S. Liu, G. Fang, J. Liang, M. Fu, B. Wang, A new type of peridynamics: Element-based peridynamics, Comput. Methods Appl. Mech. Eng. 366 (2020) 113098.

[36] J. Chen, X. Zhou, L. Zhou, F. Berto, Simple and effective approach to modeling crack propagation in the framework of extended finite element method, Theor. Appl. Fract. Mech. 106 (2020) 102452.

Nomenclature

Latin symbols

a_{ip}, b_{ip} *and* d_{ip}: PD constants of in-plane term

a_b, b_b *and* d_b: PD constants of bending term

a: half crack length

$\boldsymbol{b}$: body force vector

C_s: PD constants of shear term

E: Young's modulus

$\boldsymbol{f}$: PD force density vector

G_c: critical energy release rate

g_c: average critical energy density

$\bar{g}$: total energy density stored in each interaction bond

H_x: material points within Horizon in the PD theory

h: shell thickness

k_s: shear correction factor

K_I: mode-I stress intensity factor

K_c: critical fracture toughness

L: shell length

M: bending moment load

$\boldsymbol{m}$: mass matrix

N: total number of material points within Horizon

N_c: total number of interactions for creating a unit crack surface

p_0: pressure load

r: half distance of particle spacing

r': r-axis of the polar coordinate

s_{ip}: bond stretch of in-plane term

s_b: bond stretch of bending term

s_s: bond stretch of transverse shear term

s_c: critical bond stretch

$\boldsymbol{t}$: PD force density state

$\boldsymbol{u}=[u\ v\ w\ \theta_x\ \theta_y]^T$: displacement vector

V: volume of material point

V_0: volume of the complete horizon

W: shell width

$\bar{W}_{ip}$: strain energy density of membrane term

$\bar{W}_b$: strain energy density of bending term

$\bar{W}_s$: strain energy density of transverse shear term
$\boldsymbol{x}$: reference position vector
$\boldsymbol{x}_i$ (x_1, x_2 and x_3): x_i-axis of the coordinate system
x: position of x-axis in Cartesian coordinates
$\boldsymbol{y}$: deformation vector
y: position of y-axis in Cartesian coordinates

Greek symbols

β: crack angle
Δx: particle spacing
δ: horizon length
ζ: gradient loading
$\bar{\theta}$: rotations with respect to the interaction bond
θ': θ-axis of the polar coordinate
ϑ_{ip}: dilatation of in-plane term
ϑ_b: dilatation of bending term
κ: bulk modulus
λ: correction factor of the volume method for the surface effect
μ: shear modulus
$\mu_{(k)(j)}$: state of bond interaction between points k and j
ν: Poisson's ratio
ξ: distance between material points
ρ: mass density
σ: tensile stress
$[\sigma_{xx}\ \sigma_{yy}\ \sigma_{xy}]^T$: stress components
υ: volume correction factor
φ: angle of interaction bond with respect to the x_1-axis
ω: micro-potential
$\underline{\omega}$: influence function

Abbreviations

BC: boundary condition
CCM: classical continuum mechanics
COD: crack tip opening displacement
DLSP: diagonally loaded square plate
OSPD: ordinary state-based peridynamics
PD: peridynamics
SED: strain energy density